Planet. Space Sci., Vol. 35, No. 11, pp. 1347–1358, 1987
Printed in Great Britain.

0032–0633/87 $3.00+0.00
Pergamon Journals Ltd.

GLOBAL QUANTITATIVE MODELS OF THE GEOMAGNETIC FIELD IN THE CISLUNAR MAGNETOSPHERE FOR DIFFERENT DISTURBANCE LEVELS

N. A. TSYGANENKO
Institute of Physics, Leningrad State University, Stary Petergof 198904, Leningrad, U.S.S.R.

(*Received in final form* 5 *March* 1987)

Abstract—A previously proposed model (Tsyganenko and Usmanov, 1982, *Planet. Space Sci.* **30**, 985) is further developed, using *IMP*-A, C, D, E, F, G, H, I, J and *HEOS*-1, -2 spacecraft measurements made during 1966–1980. The main improvement consists of a considerable extension of the modeling region by adding to the original data set a large number of magnetotail field measurements. Data points used in the present study cover a vast range of distances $4 \lesssim R \lesssim 70\,R_E$ and comprise an unprecedentedly large number of measurements (a total of 36682 vector averages, almost twice as many as in our earlier data set). The data have been divided into groups corresponding to a sequence of K_p-index intervals, as well as different conditions in the solar wind. Mathematical representation of the magnetic field follows in its general features the approach developed in our earlier work, with some modifications. Two versions of the model are proposed, namely, (i) a "long" one with 26 parameters, valid up to distances $\sim 70\,R_E$, and (ii) a "truncated" one with 20 parameters and an applicability limit of $\sim 30\,R_E$.

1. INTRODUCTION

Quantitative modeling of the geomagnetic field is one of the oldest problems in geophysical research. It began with pioneering investigations by Gauss and received a considerable impetus with the beginning of space exploration, when it became necessary to develop a numerical approximation of the field valid up to distances of tens of R_E from the Earth's surface. The solution of this problem meets with difficulties stemming, in particular, from the fact that the major part of the magnetosphere is not current-free (see the review by Stern, 1976). It is thus impossible to apply the scalar potential method, for which it is enough to measure the field only at some boundary surface. The field should be measured, instead, throughout the whole modeling region, and the task is even more complex due to the extreme variability of the magnetospheric configuration, which exhibits diurnal and seasonal variations caused by the geodipole wobbling, as well as irregular fluctuations arising from substorms and other solar-wind-related phenomena. Nevertheless, sufficiently large satellite data sets make it possible to resolve the average structure of the magnetospheric field and main features of changes accompanying the increase of the geomagnetic disturbance level. This was convincingly demonstrated in the first empirical magnetospheric field models by Mead and Fairfield (1975) and by Hedgecock and Thomas (1975).

Tsyganenko and Usmanov (1982) and Usmanov (1984) proposed a more elaborate representation of the magnetic field in the near region of the magnetosphere based on a merged *IMP–HEOS* data set comprising about 19,000 vector averages. Besides correlating the field parameters with K_p and *AE* indices, deduced from ground data and gauging the disturbance level, an attempt was also made in these studies to investigate the dependence of the average magnetospheric magnetic field and current distributions upon the main geoeffective parameters of the solar wind. However, limitations of the geocentric distances of the *IMP* satellites restricted these model results to less than $\sim 15\,R_E$ down the geomagnetic tail. Recently a large amount of spacecraft magnetic field data from the cislunar magnetotail region became available to us. Merged with the original *IMP–HEOS* set, these data constituted the experimental basis for a series of "global" quantitative magnetic field models valid throughout the entire cislunar region of the Earth's magnetosphere. The present paper describes these new magnetospheric magnetic field models.

2. SPACECRAFT DATA

The data set used in this work contains a total of 36,682 points, to our knowledge the largest body of experimental information ever used in magnetospheric field modeling studies. The Mead–Fair-

field (1975) and Tsyganenko–Usmanov (1982) models have been based on, respectively, three and two times fewer data points. A data point here means a set of quantities which includes average values of three components of the external magnetic field (i.e. total field minus contribution from internal sources) together with the corresponding average values of spacecraft coordinates, the geodipole tilt angle, geomagnetic activity indices, parameters of the solar wind, and the date and universal time of observation. It should be noted here that the ground geomagnetic disturbance indices are known for most data points, whereas this is by no means the case for the solar wind parameters, due to many gaps in King's (1977) interplanetary data records. Thus, only $\sim 55\%$ of the data points contain information on the IMF, and $\sim 46\%$ have available values of solar wind velocity and density.

The whole data set includes (i) 12616 points on which the Mead–Fairfield (1975) model was based, corresponding to measurements on board the *IMP*-D, F, G and I spacecraft during 1966–1972 in the geocentric distance range $R \approx 4$–$17\ R_E$, (ii) 6248 points generated from data of *HEOS*-1 and -2 satellites taken in the range $R \approx 6$–$35\ R_E$ during 1969–1972 (Hedgecock and Thomas, 1975), (iii) 11,150 points from the data of six *IMP* spacecraft (A, C, E, F, G and I) obtained during 1964–1973 in the cislunar geomagnetic region with $-66 \lesssim x_{GSM} \lesssim -15\ R_E$, and (iv) 6675 points, derived from *IMP*-H and -J measurements made during 1973–1980 in the middle region of the cislunar tail $R \approx 25$–$45\ R_E$.

Figure 1 shows the distribution of data points along the magnetotail in $5R_E$ intervals of the x_{GSM} coordinate, for two data subsets corresponding to very quiet ($K_p = 0, 0^+$) and disturbed ($K_p \geq 4^+$) conditions. Both histograms (as well as distributions for other intervals of K_p, which are not reproduced here) are rather similar and show that most data points were obtained within the near and middle tail region, with $x_{GSM} \gtrsim -40\ R_E$, that a relatively small amount of data comes from the vicinity of the lunar orbit, and that the interval 40–45 R_E is empty.

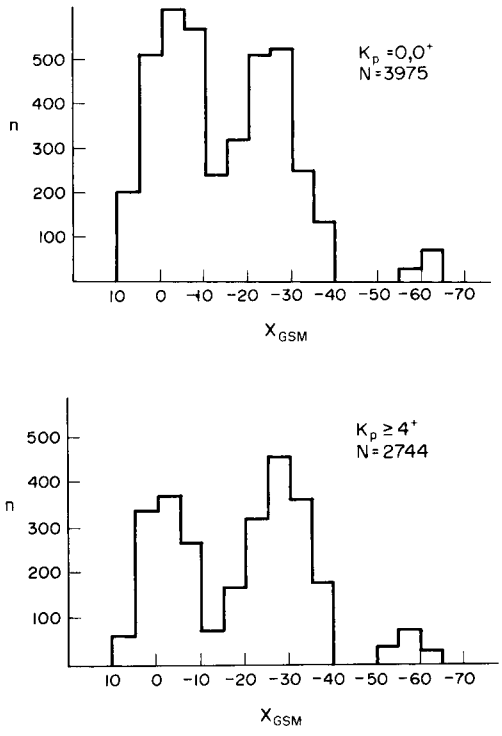

FIG. 1. DISTRIBUTIONS OF THE EXPERIMENTAL DATA POINTS IN THE 5-R_E INTERVALS OF THE x_{GSM} COORDINATE, FOR TWO DATA SUBSETS.

3. MATHEMATICAL FORMULATION OF THE MODEL

As in our previous work (Tsyganenko and Usmanov, 1982; to be referred to hereafter as Paper I), a three-term representation of the contribution from external magnetospheric sources has been adopted in the present model:

$$\mathbf{B}_e = \mathbf{B}^{(1)} + \mathbf{B}^{(2)} + \mathbf{B}^{(3)}. \tag{1}$$

The first term $\mathbf{B}^{(1)}$ gives the field of the ring current and the second one $\mathbf{B}^{(2)}$ corresponds to the magnetotail current system, including the plasma sheet current as well as return currents which confine the tail field within the lobes. The third term $\mathbf{B}^{(3)}$ yields the remaining part of the total external field, which includes the field of magnetopause currents and an averaged contribution from the large-scale system of field-aligned currents.

3.1. *The ring current term*, $\mathbf{B}^{(1)}$

This term has been taken from Paper I without any modification and hence only final expressions are given below, followed by formulae for transformation of the components of $\mathbf{B}^{(1)}$ to the solar-magnetospheric frame of reference.

In a cylindrical coordinate system (ρ, φ, ζ) with the direction aligned with geodipole axis we have

$$B_\rho = B_{RC} \frac{12\rho\zeta}{(\rho^2+\zeta^2+4)^{5/2}},$$

$$B_\zeta = 4B_{RC} \frac{2\zeta^2-\rho^2+8}{(\rho^2+\zeta^2+4)^{5/2}} \tag{2}$$

where

$$\rho = (x_{SM}^2 + y_{SM}^2)^{1/2}/R_{RC} \quad \text{and} \quad \zeta = z_{SM}/R_{RC}. \quad (3)$$

Here B_{RC} is a linear parameter of the model, which equals the magnitude of the field depression produced at the centre of the ring current, and R_{RC} is a non-linear parameter defining the scale size of the current distribution, the maximal current density corresponding to $\rho \approx 0.8$ and $\zeta = 0$ (see Paper I for details).

We suppose the ring current to be aligned with the dipole equatorial plane. Given a point (x_{GSM}, y_{GSM}, z_{GSM}) in the solar-magnetospheric system (GSM), the following calculation derives the components of the ring current field in the same system:

(i) starting from x_{GSM}, y_{GSM}, z_{GSM}, and the geodipole tilt, ψ, find the solar magnetic coordinates (z axis along dipole, xz plane contains the Sun's direction)

$$\begin{aligned} x_{SM} &= x_{GSM} \cos\psi - z_{GSM} \sin\psi \\ y_{SM} &= y_{GSM} \\ z_{SM} &= x_{GSM} \sin\psi + z_{GSM} \cos\psi, \end{aligned} \quad (4)$$

(ii) from (2)–(4) find B_ρ and B_ζ,

(iii) calculate Cartesian solar-magnetic components of $\mathbf{B}^{(1)}$:

$$B_{x,SM} = B_\rho x_{SM}/(\rho R_{RC}), \quad B_{y,SM} = B_\rho y_{SM}/(\rho R_{RC}),$$
$$B_{z,SM} = B_\zeta, \quad (5)$$

(iv) make the final transformation to the GSM system:

$$\begin{aligned} B_{x,GSM}^{(1)} &= B_{x,SM} \cos\psi + B_{z,SM} \sin\psi \\ B_{y,GSM}^{(1)} &= B_{y,SM} \\ B_{z,GSM}^{(1)} &= -B_{x,SM} \sin\psi + B_{z,SM} \cos\psi. \end{aligned} \quad (6)$$

3.2. *The magnetotail current contribution*, $\mathbf{B}^{(2)}$

As stated above, the tailward extension of the model of Paper I did not exceed ~ 15–$20\,R_E$, which made possible several simplifying assumptions. In particular, no account was made of return currents, which close the plasma sheet current in the high-latitude region and maintain the observed two-lobed structure of the geomagnetic tail. Secondly, in that model a linear approximation was adopted for the current density distribution along the tail axis.

This paper aims at providing a close approximation of the magnetic field throughout the whole cislunar region in the framework of a single mathematical model and hence the above-mentioned simplifications no longer hold in the present case. Indeed, the magnetic field gradient is much larger in the near tail region than at lunar distance (Behannon, 1970) and it is thus necessary to use a more general dependence of the plasma sheet current upon x instead of the linear approximation assumed in Paper I. As for the return current, it is quite necessary to take it into account in models with a long magnetotail in order to obtain correct distributions of both B_x and B_z components. The point here lies in that the field produced by an infinitely long rectilinear current filament varies with distance as r^{-1}, whereas the distant field from a pair of closed current loops (forming a theta-shaped circuit in the tail cross-section) decreases much more rapidly as $\sim r^{-4}$. For this reason, models with a single tail current sheet exhibit too low values of B_z in the near equatorial nightside region. Our calculations have shown that total B_z in such models becomes negative at $x_{GSM} \sim -(10$–$15)R_E$ even for lowest K_p values, in obvious contrast with reality (Behannon, 1970).

With these considerations in mind, it was finally decided to use a modified version of the approach proposed in Paper I, that is, to represent the tail current system as the result of integration over a continuous distribution of axially symmetric diffuse current filaments. The variation of the current density $I(x)$ along the tail should be approximated in this method by a rather simple function of x, leading after integration to a manageable set of analytical expressions and containing several free parameters, which allow sufficient flexibility in specifying the function

$$I = I(x) = \frac{c}{2\pi} B_T(x).$$

The following dependence was chosen in the present study:

$$B_T(x) = B_0 + \frac{B_1}{x - x_1} + \frac{B_2}{(x - x_2)^2} \quad (7)$$

with three linear parameters (B_0, B_1, B_2) and two non-linear ones (x_1, x_2). Assuming an infinite extension of the current sheet in the directions $y \to \pm\infty$ and $x \to -\infty$, we have for the magnetic field components:

$$B_x^{(2)}(x,z) = \frac{z}{\pi} \int_{-\infty}^{x_N} B_T(x_0) \frac{dx_0}{(x_0 - x)^2 + z^2 + D^2} \quad (8)$$

$$B_z^{(2)}(x,z) = \frac{1}{\pi} \int_{-\infty}^{x_N} B_T(x_0) \frac{(x_0 - x)\,dx_0}{(x_0 - x)^2 + z^2 + D^2} \quad (9)$$

where x_N defines the location of the inner edge of the current sheet and D gives its half-thickness scale. In Paper I the distant limit of integration had a finite value x_F, to avoid diverging integrals. Here whenever such a divergence could occur it is cancelled by the return current system and hence $x_F = -\infty$ is used.

The return current system is simulated by a pair of additional current sheets parallel to the central one and located at $z_{GSM} = \pm R_T$ above and below the equatorial plane, where $R_T = 30\,R_E$ is taken of the order of asymptotic tail radius. Each sheet carries an eastward current with density $-\frac{1}{2}I(x)$, i.e. minus half of that in the main current sheet.

Following Paper I, in order to restrict the current sheet width in the dawn–dusk direction both field components (8) and (9) are multiplied by an even function $f(y)$ which falls off to zero by $y \to \pm\infty$ with a scale length $\Delta y \sim 15\,R_E$. This bends current flow lines near the inner edge of the sheet, so that a smooth continuous transition occurs in the current flow line distribution from the ring current to the plasma sheet. In the magnetotail cross-section we obtain two closed current loops, which form the well-known theta-shaped structure encircling the tail lobes.

As in Paper I, a shift in z of the whole central current sheet by $z_S = R_H \sin\psi$ has been introduced to take into account the effects of the geodipole tilt.

As a result, the field components $B_x^{(2)}(x,y,z)$ and $B_z^{(2)}(x,y,z)$ are given by the following calculations (as in Paper I, this tail current model does not contribute to the B_y-component of the total field). Let us introduce

$$\xi_1 = x_1 - x, \quad \xi_2 = x_2 - x, \quad \xi_N = x_N - x$$

$$z_r = z - R_H \sin\psi, \quad z_+ = z - R_T, \quad z_- = z + R_T$$

$$\beta(z_r) = (z_r^2 + D^2)^{1/2}, \quad \beta_+ = (z_+^2 + D^2)^{1/2},$$

$$\beta_- = (z_-^2 + D^2)^{1/2}$$

$$\gamma_1(\beta) = \xi_1^2 + \beta^2, \quad \gamma_{1\pm} = \gamma_1(\beta_\pm)$$

$$\gamma_2(\beta) = \xi_2^2 + \beta^2, \quad \gamma_{2\pm} = \gamma_2(\beta_\pm)$$

$$P_1(\gamma_1, \beta) = \frac{1}{2\gamma_1} \ln \frac{(x_N - x_1)^2}{\xi_N^2 + \beta^2},$$

$$P_2(\gamma_2, \beta_2) = \frac{1}{\gamma_2^2} \ln \frac{(x_N - x_2)^2}{\xi_N^2 + \beta^2}$$

$$P_{1\pm} = P_1(\gamma_{1\pm}, \beta_\pm), \quad P_{2\pm} = P_2(\gamma_{2\pm}, \beta_\pm). \tag{10}$$

Then we find

$$S_0 = \beta^{-1}[\pi/2 + \arctan(\xi_N/\beta)]$$

$$S_1 = P_1 - (\xi_1/\gamma_1) S_0$$

$$S_2 = -\xi_2 P_2 - \frac{1}{(x_N - x_2)\gamma_2} + \frac{\xi_2^2 - \beta^2}{\gamma_2^2} S_0$$

$$G_0 = \frac{1}{2} \ln \frac{\xi_N^2 + \beta^2}{[(\xi_N^2 + \beta_+^2)(\xi_N^2 + \beta_-^2)]^{1/2}}$$

$$G_1 = \frac{\beta^2}{\gamma_1} S_0 + \xi_1 P_1 \tag{11}$$

$$G_2 = \frac{\beta^2 - \xi_2^2}{2} P_2 - \frac{2\beta^2 \xi_2}{\gamma_2^2} S_0 - \frac{\xi_2}{(x_N - x_2)\gamma_2}. \tag{12}$$

We also derive quantities $S_{0\pm}$, $S_{1\pm}$, $S_{2\pm}$, $G_{1\pm}$, $G_{2\pm}$, given by (11) with substitutions $\beta \to \beta_\pm$, $\gamma_{1,2} \to \gamma_{1,2\pm}$, $P_{1,2} \to P_{1,2\pm}$, $S_0 \to S_{0\pm}$. After that we can write down final expressions for the model magnetotail field components

$$B_x^{(2)}(x,y,z) = f(y)\{B_0[z_r S_0 - \tfrac{1}{2}(z_+ S_{0+} + z_- S_{0-})] + B_1[z_r S_1 - \tfrac{1}{2}(z_+ S_{1+} + z_- S_{1-})] + B_2[z_r S_2 - \tfrac{1}{2}(z_+ S_{2+} + z_- S_{2-})]\}$$

$$B_y^{(2)} = 0$$

$$B_z^{(2)}(x,y,z) = f(y)\{B_0 G_0 + B_1[G_1 - \tfrac{1}{2}(G_{1+} + G_{1-})] + B_2[G_2 - \tfrac{1}{2}(G_{2+} + G_{2-})]\} \tag{12}$$

where

$$f(y) = \frac{1}{\pi}[1 + (y/\Delta y)^2]^{-1}. \tag{13}$$

3.3. *Approximation for the term* $\mathbf{B}^{(3)}$

This part of the external field was represented in Paper I by polynomials in y and z, also containing an exponential term in x and the sine of the geodipole tilt angle ψ. A similar approach is retained in the present model, with some modifications, leading to components

$$B_x^{(3)} = e^{x/\Delta x_1}[a_1 z \cos\psi + a_2 \sin\psi] + e^{x/\Delta x_2}[a_3 z \cos\psi + (a_4 + a_5 y^2 + a_6 z^2)\sin\psi]$$

$$B_y^{(3)} = e^{x/\Delta x_1}[b_1 yz \cos\psi + b_2 y \sin\psi] + e^{x/\Delta x_2}[b_3 yz \cos\psi + (b_4 y + b_5 y^3 + b_6 yz^2)\sin\psi]$$

$$B_z^{(3)} = e^{x/\Delta x_1}[(c_1 + c_2 y^2 + c_3 z^2)\cos\psi + c_4 z \sin\psi] + e^{x/\Delta x_2}[(c_5 + c_6 y^2 + c_7 z^2)\cos\psi + (c_8 z + c_9 z y^2 + c_{10} z^3)\sin\psi]. \tag{14}$$

Six additional relations follow from requirement $\nabla \cdot \mathbf{B} = 0$ imposed on (14):

$$a_1/\Delta x_1 + b_1 + 2c_3 = 0$$

$$a_2/\Delta x_1 + b_2 + c_4 = 0$$

$$a_3/\Delta x_2 + b_3 + 2c_7 = 0$$

$$a_4/\Delta x_2 + b_4 + c_8 = 0$$

$$a_5/\Delta x_2 + 3b_5 + c_9 = 0$$

$$a_6/\Delta x_2 + b_6 + 3c_{10} = 0. \tag{15}$$

In contrast with Paper I, the coordinates x, y, z refer here to the solar-magnetospheric frame of reference

rather than solar-magnetic one, because of a significantly larger tailward extension of the modeling region in the present study. Each right-hand side term in (14) is proportional to either cos ψ or to sin ψ, each containing only those powers of y and z which satisfy the symmetry conditions for, respectively, perpendicular ($\psi = 0$) and parallel ($\psi = \pi/2$) orientation of the geodipole. Besides that, each sum in (14) is divided into two parts with different scales of exponential factors, Δx_1 and Δx_2. Terms with exp $(x/\Delta x_1)$ have a larger variation scale along the x-axis ($\Delta x_1 \sim 25\, R_E$) and the corresponding polynomials in y and z are of the first order. The second variation scale, Δx_2, was chosen to be half as large as the first one ($\Delta x_2 = 0.5\Delta x_1$) and the corresponding polynomials contain terms up to the third degree. The terms containing Δx_2 were introduced in order to resolve finer details from the large-scale background field of the magnetopause current system. An estimation of the errors in the computed model coefficients a_1–c_{10} has shown that their uncertainty does not exceed a few tens of per cent and hence such a detailed representation seems to be warranted.

4. RESULTS: A "LONG" VERSION OF THE MODEL

To develop sets of coefficients corresponding to different disturbance levels, the following data subsets were created from the general data pool: (1) $K_p = 0, 0^+$, (2) $K_p = 1^-, 1, 1^+$, (3) $K_p = 2^-, 2, 2^+$, (4) $K_p = 3^-, 3, 3^+$, (5) $K_p = 4^-, 4, 4^+$, (6) $K_p \geqslant 5^-$. In three cases (subsets 2, 3 and 4) the corresponding numbers of points appeared to be too large (respectively, 9977, 9848 and 7309) and therefore an additional consolidation procedure was applied to these subsets. The procedure selected close groups of points separated from each other by $\Delta R \leqslant 1\, R_E$ and corresponding to values of the geodipole tilt angle within a range $\Delta\psi = 6°$, then it calculated for each group average values of coordinates, tilt angle and field components, and assigned to them statistical weights proportional to the number of contributing points. The average number of points per group was found to be ≈ 2.3, with the total number of groups of the order of 2000–3000.

As can be seen from Section 3, the model contains 26 linear parameters a_1–a_6, b_1–b_6, c_1–c_{10}, B_0, B_1, B_2, and B_{RC}, of which only 20 are independent, and 10 non-linear parameters R_{RC}, x_N, D, Δy, R_H, Δx_1, Δx_2, x_1, x_2, R_T, of which the last three were chosen with constant values, in accordance with general properties of the magnetotail configuration. Thus after preliminary calculations it was decided to choose $x_1 = 4\, R_E$ and $x_2 = 5\, R_E$ in order to match the variation of $B_T(x)$ given by (7) with that of the average magnetic field along the tail as obtained by Behannon (1970). Computations have shown that the three linear parameters B_0, B_1, B_2 in (7) provide sufficient flexibility of the function $B_T(x)$ and allow the remaining non-linear parameters x_1 and x_2 to be held fixed.

The parameter R_T, the distance from the GSM equatorial plane to the upper and lower magnetotail return current sheets, was also given a fixed value $R_T = 30\, R_E$. As for the second scaling length Δx_2 in (14), it was taken as $\Delta x_2 = 0.5\, \Delta x_1$ and hence does not vary independently.

Therefore, a total of 20 linear and six non-linear parameters had to be determined from each data subset. An iterative code was developed for this purpose which in each data subset minimized the r.m.s. deviation σ of the model field from the experimental data. Before beginning the iterative process, initial tentative values of non-linear parameters were specified. After that, the first approximation values for all linear parameters were computed by means of a standard least-squares routine. The next step was a search for optimal values of the non-linear parameters using the Newton–LeCam–Marquardt method (Usmanov, 1984), the linear parameters remaining fixed at the previously found values. This completed the first iteration, and the whole sequence of calculations was then repeated again. As in Paper I, four iterations appeared quite sufficient, since the main decrease in σ was in most cases obtained in the first two or three cycles.

The values of model parameters derived for the data subsets listed above, corresponding to six intervals of the K_p-index, are given in Table 1, except for the fixed parameters $x_1 = 4$, $x_2 = 5$, $R_T = 30$, and also $\Delta x_2 = 0.5\Delta x_1$. All distances are in Earth radii and all field intensities in nanoteslas.

The first lines of Table 1 contain the following characteristics of the data subsets: the number N of points (in cases where the consolidation procedure was applied, the final numbers of points are given in brackets), the average magnitude $\langle B_e \rangle$ of the external field and the r.m.s. deviation σ of the model from the data. As can be seen, the number of data points is largest for quiet conditions and decreases rapidly with increasing activity level. Quantities $\langle B_e \rangle$ and σ grow monotonically with the increase of K_p; however, their ratio $\langle B_e \rangle / \sigma$ remains nearly constant about ≈ 2.2.

About a half of the model parameters show a systematic change with growing K_p (either monotonic or with one extremum at moderate disturbance levels). The remaining parameters change more irregularly, though within a rather limited range of values. Our least-squares procedure made it possible to evaluate the errors for all calculated parameters, under the

TABLE I

K_p	$0, 0^+$	$1^-, 1, 1^+$	$2^-, 2, 2^+$	$3^-, 3, 3^+$	$4^-, 4, 4^+$	$\geqslant 5^-$
N	3975	9977 (5731)	9848 (5722)	7309 (4236)	3723	1850
$\langle B_e \rangle$	15.49	18.86	21.54	25.27	28.58	32.88
σ	6.70	8.37	9.72	11.53	12.70	15.65
a_1	−0.09673	−0.4850	−1.132	−1.003	−1.539	−2.581
a_2	−10.63	−12.84	−18.05	−16.98	−14.29	−7.726
a_3	1.210	1.856	2.625	3.140	3.479	5.045
a_4	34.57	40.06	48.55	52.81	53.36	53.31
a_5	−0.04502	−0.0294	−0.004868	−0.08625	−0.004201	0.02262
a_6	−0.06553	−0.09071	−0.1087	−0.1478	−0.2043	−0.1972
b_1	−0.02952	−0.02993	−0.03824	−0.03501	−0.03932	−0.01981
b_2	0.3852	0.5465	0.8514	0.5500	0.6409	0.4280
b_3	−0.03665	−0.04928	−0.0522	−0.07778	−0.1058	−0.1055
b_4	−2.084	−2.453	−2.881	−2.970	−3.221	−5.075
b_5	0.001795	0.001587	−0.000295	0.002086	−0.00114	0.002762
b_6	0.00638	0.007402	0.009055	0.01275	−0.02166	0.03277
c_1	−23.49	−29.41	−29.48	−26.79	−30.43	−27.35
c_2	0.06082	0.08101	0.06394	0.06328	0.04049	0.04986
c_3	0.01642	0.02322	0.03864	0.03622	0.05464	0.06119
c_4	−0.02137	−0.1091	−0.2288	0.08345	0.008884	−0.1211
c_5	32.21	40.75	41.77	39.72	42.00	47.48
c_6	−0.04373	−0.07995	−0.05849	−0.06009	−0.01035	−0.0502
c_7	−0.02311	−0.03859	−0.06443	−0.07825	−0.1053	−0.1477
c_8	−0.2832	−0.2755	−0.4683	−0.9698	−1.630	0.838
c_9	−0.002303	−0.002759	0.001222	0.000178	0.003802	−0.01008
c_{10}	−0.000631	−0.000408	−0.000519	−0.000573	−0.001029	−0.0057
B_0	−6.397	−6.189	−3.696	−0.9328	4.204	9.231
B_1	−967.0	−957.8	−991.1	−872.5	−665.6	−674.3
B_2	−8650.0	−7246.0	−6955.0	−5851.0	−1011.0	−900.0
B_{RC}	−20.55	−25.51	−31.43	−39.68	−43.49	−74.43
R_{RC}	5.180	5.207	4.878	4.902	4.514	4.658
x_N	−2.796	−4.184	−3.151	−3.848	−2.948	−3.245
D	2.715	2.641	3.277	2.790	2.99	3.39
Δy	13.58	16.56	19.19	20.91	21.59	21.80
R_H	8.038	7.795	7.248	6.193	6.005	5.620
Δx_1	29.21	29.36	28.99	26.81	22.00	25.17

assumption of a random "noise" field with a normal distribution superimposed on the regular magnetospheric average structure. Besides that, the correlation matrix was computed, containing quantitative information on the degree of statistical independence of each pair of model parameters and also a measure of their resolvability using the information in their data set. In the present case the errors for most parameters were found not to exceed a few tens of per cent, and correlation coefficients for them did not exceed 0.2–0.4. However, the pairs a_1–a_3, a_2–a_4, b_1–b_3, b_2–b_4, c_1–c_5, c_2–c_4, c_3–c_6 and c_4–c_8 showed larger correlations (0.5–0.8), because the corresponding terms in (14) differed only in scale lengths of the exponential factors.

Most trends in the parameters and in the model magnetic field which accompany an increase in the K_p-index are similar to those reported in Paper I. These include (i) a distinct monotonic increase in the ring current intensity from $B_{RC} = -20.55$ nT ($K_p = 0, 0^+$) up to $B_{RC} = -74.43$ nT ($K_p \geqslant 5^-$), (ii) a decrease of the "hinging distance" R_H from 8.04 R_E down to 5.62 R_E. The current sheet half-thickness D, in line with results of Paper I, does not show any systematic changes, being in all cases of the order of 3 R_E. In one of the preliminary versions of the model an attempt was made to include the variation of the current sheet thickness with the distance x along the tail. For this purpose it was assumed that $D(x) = (c_1 + c_2 x)^{1/2}$ in (8) and (9), this modification leading to slightly more cumbersome expressions in the final formulae. Computations showed that σ was smallest for $c_2 \approx -0.07$. This suggests that the average thickness of the sheet grows slowly in the tailward direction: for $x = -10\ R_E$, $D \sim 2.5\ R_E$, whereas near the lunar orbit $D \sim 3.5\ R_E$. The most likely reason for such a result is the transverse flapping motion of the sheet, which has a much larger amplitude in the

remote tail region than at closer distances. In the average model this is manifested in an apparent thickening of the current sheet towards larger distances.

Note that in the present work both the ring current intensity B_{RC} and its radius R_{RC} were treated as variable parameters (in Paper I, R_{RC} had a fixed value $R_{RC} = 4\,R_E$ for all K_p intervals). Judging from the obtained error values (typically 5–10%), this parameter can be resolved quite effectively and evidently tends to decrease with increasing disturbance.

As concerns the scale width of the tail current sheet Δy, its behaviour as derived in Paper I differs from that found for the "long" version of the present model. It can be seen from Table 1 that Δy increases steadily and reaches the value of $\Delta y = 21.80$ by $K_p \geqslant 5^-$, whereas in our earlier study (Paper I) an increase of Δy in the low activity range was followed by its decrease towards highest K_p values. In the "truncated" version of the present model which takes into account only near-tail data with $x_{SM} \geqslant -25\,R_E$ (see below), the same non-monotonic behaviour of Δy vs K_p was obtained. This implies that the steady increase of Δy in the "long" model can be traced to the large number of data points from the region $-40 \lesssim x_{GSM} \lesssim -25\,R_E$ and manifests a widening of the current sheet (and/or lesser curvature of the current flow lines) in this part of the magnetotail during disturbed periods. In the near region of the nightside magnetosphere the opposite effect of enhanced compression seems to dominate, since a distinct trend to decrease can be observed both in Δy and Δx (see Table 2 of the next section). The "long" model does not allow one to account for both effects; this is one of its shortcomings.

Figures 2–4 show plots of magnetic field lines for two extreme options of the "long" model, corresponding to very quiet ($K_p = 0, 0^+$) and strongly disturbed ($K_p \geqslant 5^-$) conditions, and also the field line configuration for a tilted geodipole with $\psi = 30°$.

Figure 5 shows several profiles of the magnetotail current density, given by the function $B_T(x)$ in (7), for different disturbance levels. Increase of the K_p-index is accompanied by a significant and almost monotonic rise of the current throughout the whole range of distances. In the near region a clear tendency to an earthward shift of the current maximum is also easily seen, so that the curves for $K_p = 4^-, 4, 4^+$ and $K_p \geqslant 5^-$ show a purely monotonic decrease of the current in the tailward direction. In the limit $D \to 0$, $2B_T(x)$ is the difference in B_x between opposite sides of the plasma sheet and therefore $B_T(x)$ at any given x is expected to approximate the intensity of the lobe field. Curves for $K_p = 0, 0^+$ and $K_p = 1^-, 1, 1^+$ are indeed in good agreement with earlier results by Behannon (1970), which gave $B \sim 20$ nT near $x_{GSM} \sim -20\,R_E$, and $B \sim 8$–10 nT near the Moon's orbit.

5. A "TRUNCATED" VERSION OF THE MODEL

In many cases it is not necessary to extend model calculations of the magnetic field down the tail further than $R \sim 25$–$30\,R_E$. For that purpose a series of

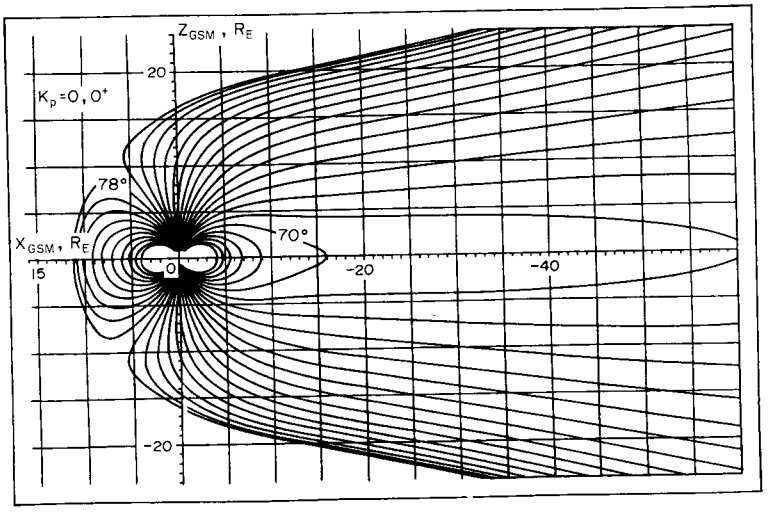

FIG. 2. FIELD LINE PATTERN IN THE NOON–MIDNIGHT MERIDIAN PLANE, CORRESPONDING TO VERY QUIET CONDITIONS ($K_p = 0, 0^+$) IN THE "LONG" VERSION OF THE MODEL.
Field lines start from Earth at latitudes 2° apart, beginning from 60°.

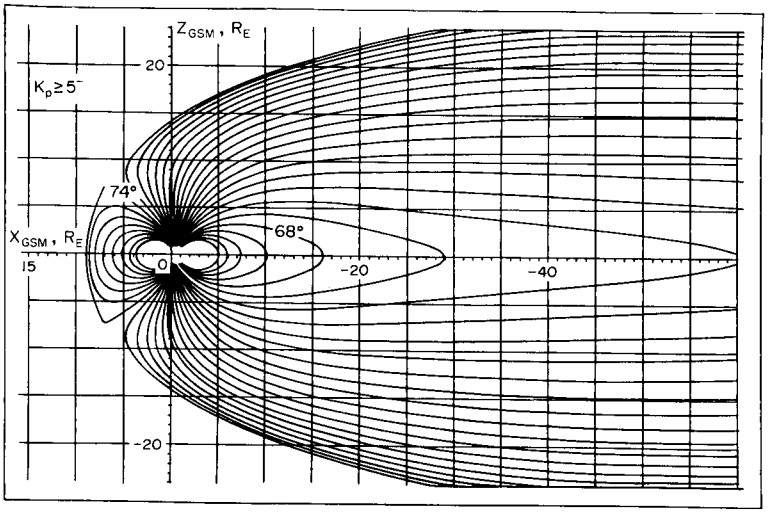

FIG. 3. FIELD LINE PATTERN IN THE "LONG" VERSION OF THE MODEL FOR STRONGLY DISTURBED CONDITIONS WITH $K_p \geq 5^-$.

"truncated" models was developed, based on experimental data points with $x_{SM} \geq -25 R_E$. The significantly shorter range of distances allows the following simplifications: (i) the third term in (7) is deleted by putting $B_2 = 0$ and thus eliminating all the terms with the subscript 2 in final expressions (10)–(12), and (ii) only terms with the scale length Δx_2 (relabeled Δx) are retained in the right-hand sides of (14), which can now be rewritten as

$$B_x^{(3)} = e^{x/\Delta x}[a_1 z \cos\psi + (a_2 + a_3 y^2 + a_4 z^2) \sin\psi]$$
$$B_y^{(3)} = e^{x/\Delta x}[b_1 yz \cos\psi + (b_2 y + b_3 y^3 + b_4 yz^2) \sin\psi]$$
$$B_z^{(3)} = e^{x/\Delta x}[(c_1 + c_2 y^2 + c_3 z^2) \cos\psi + (c_4 z + c_5 zy^2 + c_6 z^3) \sin\psi]. \quad (16)$$

One more change concerns the non-linear parameter x_1 in (7), which in this case was allowed to

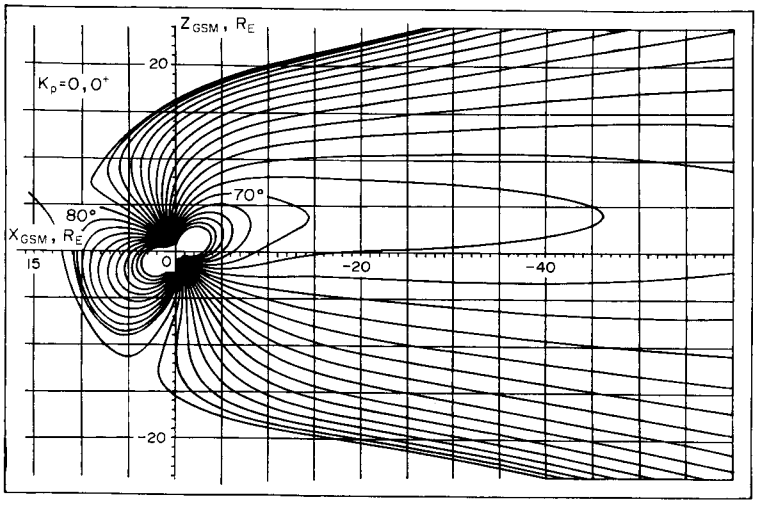

FIG. 4. FIELD LINE PATTERN IN THE "LONG" VERSION OF THE MODEL FOR A TILTED GEODIPOLE ($\psi = 30^\circ$) AND VERY QUIET CONDITIONS ($K_p = 0, 0^+$).

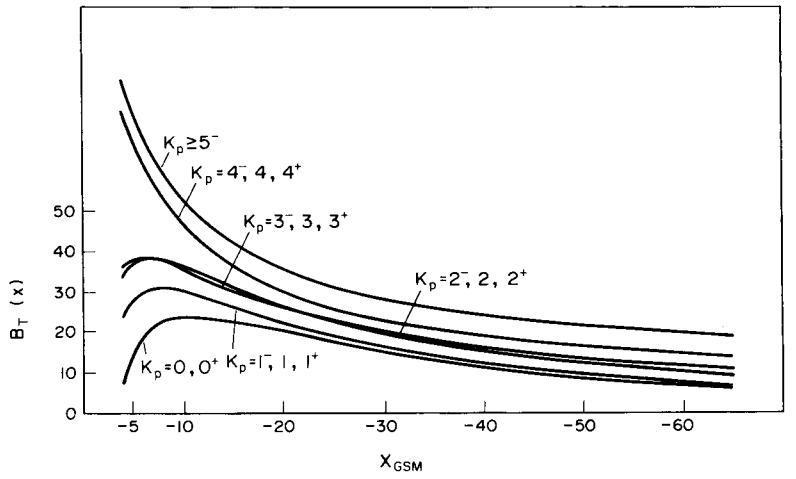

FIG. 5. PLOTS OF THE MAGNETOTAIL CURRENT FUNCTION $B_T(x)$ (IN NANOTESLAS) GIVEN BY (7), WITH COEFFICIENTS CORRESPONDING TO DIFFERENT DISTURBANCE LEVELS.

vary. Later it became evident that this modification was not necessary and that in the "truncated" range of distances it was quite sufficient to vary only the two linear parameters B_0 and B_1. This was also corroborated by the fact that the coefficients of correlation of x_1 with B_0 and B_1 were found to be unexpectedly high (0.95–0.98) and that the error estimates for x_1 exceeded those for other parameters by an order of magnitude or even more. For the same reason an enhanced scatter is seen in the values of x_1 and B_1 listed below in Table 2. Nevertheless, this scatter does not affect the resultant distribution of the tail current

TABLE 2

K_p	$0, 0^+$	$1^-, 1$	$1^+, 2^-$	$2, 2^+$	$3^-, 3, 3^+$	$4^-, 4, 4^+$	$\geq 5^-$	$\geq 5^+$
N	2556	3948	4000	3728	4275	1905	862	378
$\langle B_e \rangle$	17.41	21.26	24.46	25.97	30.88	36.03	42.62	44.31
σ	7.63	9.95	11.36	12.17	14.37	15.72	20.18	22.69
a_1	1.126	1.403	1.589	1.699	2.141	2.252	2.773	2.919
a_2	26.66	29.24	31.07	36.28	41.51	39.35	40.95	34.96
a_3	−0.077	−0.0693	−0.06527	−0.07514	−0.1518	−0.04525	0.00667	0.0*
a_4	−0.06102	−0.0864	−0.07447	−0.1448	−0.1857	−0.2062	−0.133	0.0*
b_1	−0.06197	−0.07202	−0.07632	−0.08049	−0.1015	−0.1491	−0.1304	−0.1609
b_2	−2.048	−2.068	−2.413	−2.209	−2.929	−3.059	−5.187	−5.077
b_3	0.00327	0.00286	0.002719	0.000919	0.004584	−0.000183	0.004623	0.0*
b_4	0.008473	0.007438	0.01098	0.01084	0.01589	0.02614	0.03651	0.0*
c_1	12.72	16.37	16.20	17.38	18.29	15.48	20.0	22.1
c_2	−0.00867	−0.02705	−0.02355	−0.03516	−0.02514	−0.02144	−0.03765	−0.05915
c_3	−0.001953	−0.0281	−0.03475	−0.03886	−0.05927	−0.06608	−0.09066	−0.1051
c_4	−0.3437	−0.6040	−0.4377	−1.169	−1.336	−1.855	0.5838	0.6321
c_5	−0.002903	−0.002256	−0.002169	0.004239	0.00185	0.006199	−0.01462	0.0*
c_6	−0.000999	0.000152	−0.001383	0.000881	0.001066	−0.00013	−0.007189	0.0*
B_0	18.41	20.20	18.70	21.79	21.31	23.91	24.87	28.11
B_1	−270.3	−140.1	−292.6	−162.0	−358.8	−161.0	−186.07	−330.1
B_{RC}	−25.94	−29.65	−35.25	−41.87	−47.91	−51.48	−74.81	−86.82
R_{RC}	5.21	5.62	5.29	5.15	5.13	4.61	4.57	4.00
x_N	−6.20	−5.52	−5.18	−3.62	−3.74	−3.32	−4.03	−3.00*
D	2.29	2.02	2.21	2.35	2.07	1.68	1.70	1.73*
Δy	11.96	14.66	14.03	17.26	17.23	15.22	12.15	12.56
R_H	8.315	8.06	7.66	7.61	6.33	6.68	6.87	5.11
x_1	44.22	27.76	17.56	17.99	32.51	0.6765	−1.746	4.0*
Δx	11.15	10.94	10.90	10.74	9.73	8.007	8.9	7.866

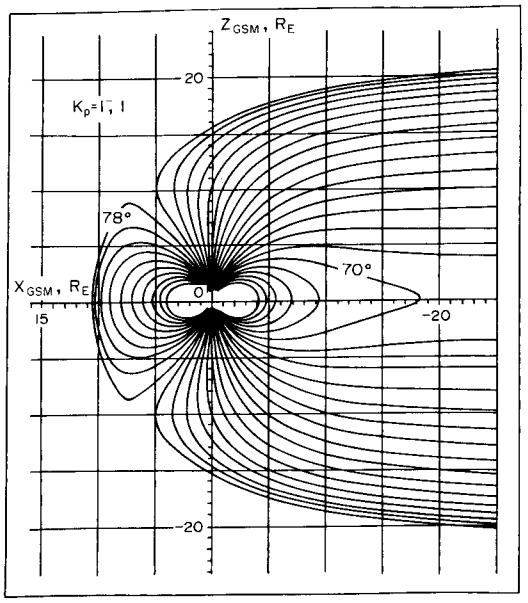

FIG. 6. FIELD LINE PATTERN IN THE "TRUNCATED" VERSION OF THE MODEL, FOR QUIET CONDITIONS WITH $K_p = 1^-, 1$.

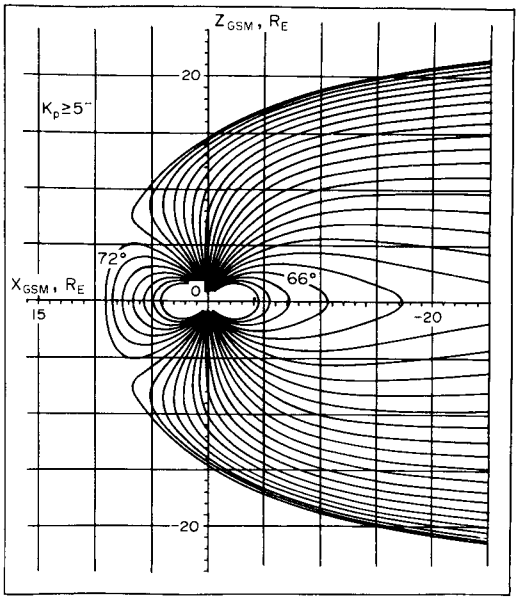

FIG. 8. FIELD LINE PATTERN IN THE "TRUNCATED" VERSION OF THE MODEL; STRONGLY DISTURBED CONDITIONS WITH $K_p \geq 5^-$.

defined by (7) and hence the model field. On that ground it was decided not to recalculate the model parameters with a fixed value of x_1.

The results are given in Table 2. As can be seen, a more detailed division of the K_p-index scale was used here in sorting the data points into separate subsets. Also, one additional set of model parameters was computed, corresponding to the most disturbed con-

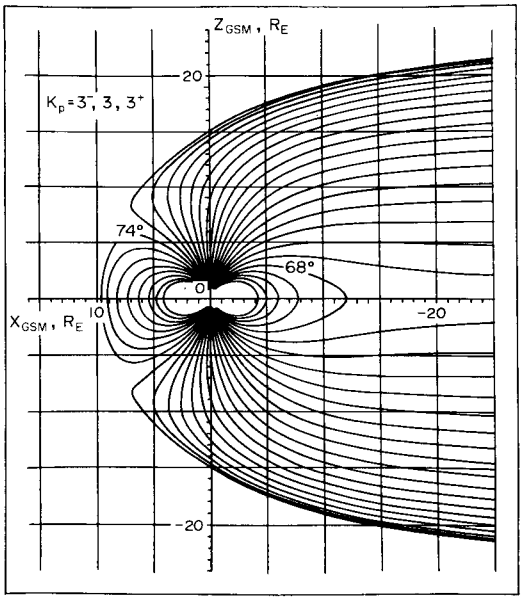

FIG. 7. FIELD LINE PATTERN IN THE "TRUNCATED" VERSION OF THE MODEL; MODERATELY DISTURBED CONDITIONS WITH $K_p = 3^-, 3, 3^+$.

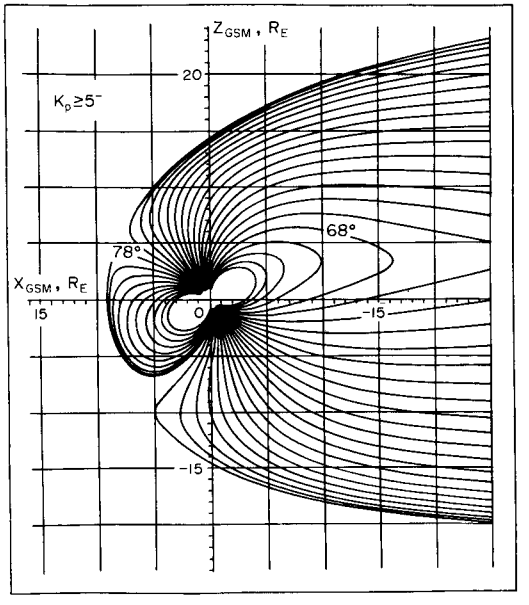

FIG. 9. FIELD LINE PATTERN IN THE "TRUNCATED" VERSION OF THE MODEL; $K_p \geq 5^-$ AND TILTED GEODIPOLE.

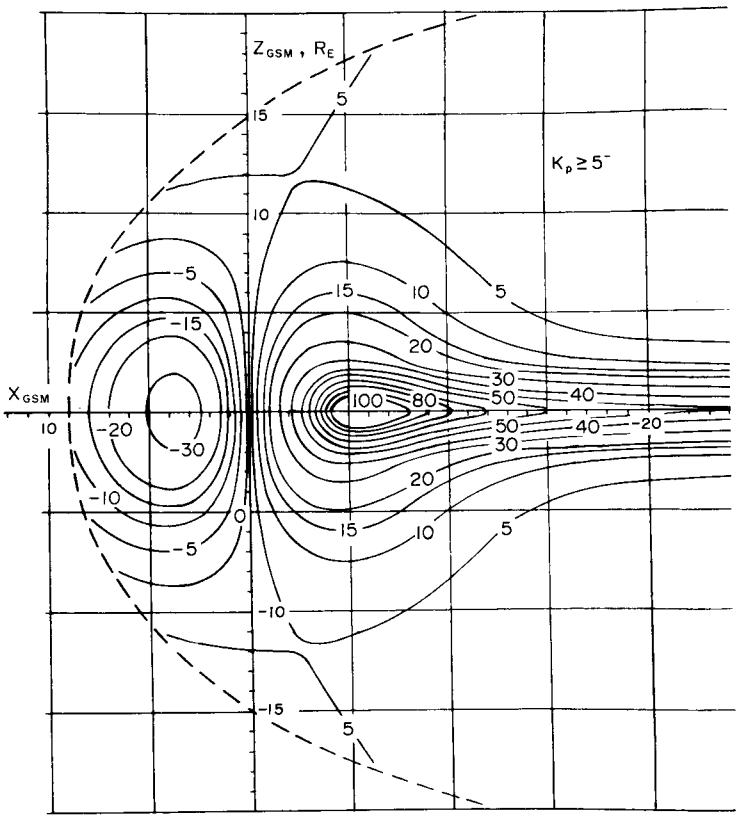

FIG. 10. CONTOURS OF CONSTANT ELECTRIC CURRENT DENSITY, j_y, IN THE NOON–MIDNIGHT MERIDIAN PLANE AS OBTAINED FROM $\nabla \times \mathbf{B}$.
The contours are labeled in units of 10^{-10} A m^{-2}; positive values correspond to a dawn–dusk direction of the current (nightside region). Broken line marks the approximate position of the model magnetopause.

ditions with $K_p \geqslant 5^+$, besides the one with $K_p \geqslant 5^-$. In this case only $N = 378$ points were found for the data subset; that is why the non-linear parameters D and x_1 were fixed at constant values and several higher-order terms in (16) were eliminated (corresponding values in Table 2 are marked with asterisks).

Figures 6–9 show the field line configurations in the "truncated" version of the model, for $K_p = 1^-, 1$, $K_p = 3^-, 3, 3^+$ and $K_p \geqslant 5^-$. As in Figs 2 and 3, the main effects of increased disturbance, easily seen in the average model field structure, are the equatorward displacement of dayside polar cusps from latitude $\approx 79°$ up to $\approx 73°$ and some stretching of the near-tail field lines. The last effect, as calculations of B_x and B_z have shown, occurs mainly due to an increase of B_x outside the current sheet, rather than a decrease of B_z. In the plasma sheet B_z does not exhibit any pronounced changes in that region, and at greater distances it even increases slightly, as demonstrated by Figs 2 and 3. It is natural to suppose that the increase of average B_x in the tail lobes during intervals of higher K_p comes from enhancement of the solar wind pressure and from growth of the tail magnetic flux due to a greater rate of reconnection on the day side. On the other hand, variations in the average B_z distribution in the nightside magnetosphere are determined by a superposition of general tail current increases during disturbed periods (which decreases B_z within the near tail region) and sporadic events of abrupt positive excursions of B_z caused by a rapid dipolization of the tail structure observed during the active phase of substorm.

The question of the average tail field distribution requires an additional "local" model study, the results of which will be reported in a separate paper.

To illustrate the overall distribution of electric current density in the model, a family of j_y isolines computed by taking the curl of the model field is shown in Fig. 10. This map refers to disturbed conditions with $K_p \geqslant 5^-$; on the nightside the tail current and

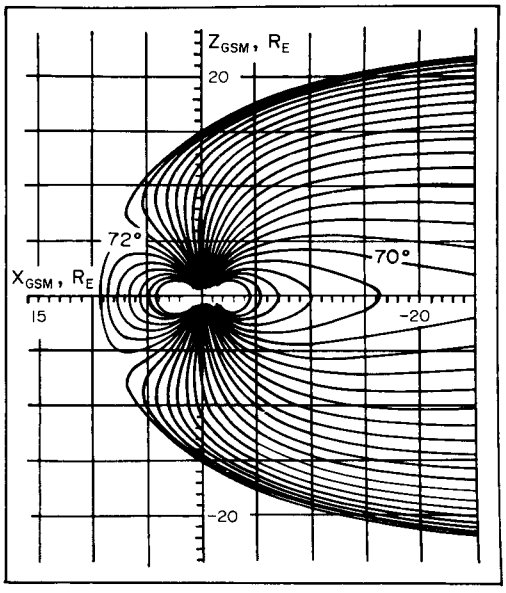

FIG. 11. FIELD LINE PATTERN OBTAINED IN THE "TRUNCATED" MODEL FROM A DATA SUBSET CORRESPONDING TO STRONGLY SOUTHWARD IMF: $B_z^{IMF} < -4$ nT, AND $|B_y^{IMF}| < 3$ nT.

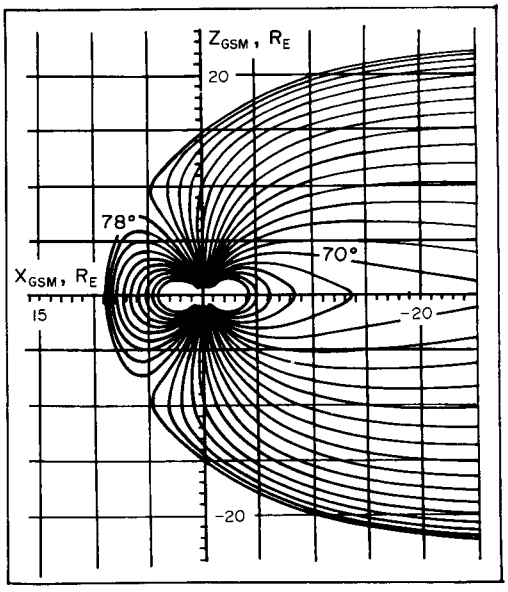

FIG. 12. THE SAME AS IN FIG. 11, BUT FOR A STRONGLY NORTHWARD IMF: $B_z^{IMF} \geqslant 4$ nT, $|B_y^{IMF}| < 3$ nT.

ring current merge together, so that j_y exceeds 10^{-8} A m^{-2} and sharp gradients of the current density are present in the vicinity of the plasma sheet. On the dayside a much more gradual variation of j_y is observed with a peak value of 3×10^{-9} A m^{-2} near the ring current maximum at $R \sim 3.5\,R_E$.

Two more examples of the average magnetospheric configurations are given in Figs 11 and 12. They correspond to "truncated" models obtained from two data subsets, in which the interplanetary North–South component was, respectively, large and negative ($B_z^{IMF} < -4$ nT) or large and positive ($B_z^{IMF} \geqslant 4$ nT). In both cases an additional limitation $|B_y^{IMF}| < 3$ nT was also imposed, to rule out B_y-related effects. As can be seen, even the average structures demonstrate a clear re-distribution of the magnetic flux between the dayside sector and tail lobes.

As a final remark to this section, a note should be made that for higher K_p levels the "truncated" model gives better results than the "long" version in the dawn and dusk sectors of the near magnetotail region, because of significantly smaller values of the dimension scale Δy, as has already been discussed in the end of Section 4. The "truncated" model is thus recommended as the preferential one for use in the region $x_{GSM} \gtrsim -30\,R_E$.

Acknowledgement—I am grateful to Dr A. V. Usmanov for the use of his subroutines and helpful discussions. The *IMP* magnetic data and Interplanetary Medium Data have been provided by WDC-A for Rockets and Satellites. I also thank Dr P. C. Hedgecock for the use of *HEOS* magnetic field data, and the Referee for careful examination of manuscript and helpful comments.

REFERENCES

Behannon, K. W. (1970) Geometry of the geomagnetic tail. *J. geophys. Res.* **75**, 743.

Hedgecock, P. C. and Thomas, B. (1975) *HEOS* observations of the configuration of the magnetosphere. *J. R. astr. Soc.* **41**, 391.

King, J. H. (1977) *Interplanetary Medium Data Book*. Rept NSSDC 77-04a, Greenbelt.

Mead, G. D. and Fairfield, D. H. (1975) A quantitative magnetospheric model derived from spacecraft magnetometer data. *J. geophys. Res.* **80**, 523.

Stern, D. P. (1976) Representation of magnetic fields in space. *Rev. Geophys. Space Phys.* **14**, 199.

Tsyganenko, N. A. and Usmanov, A. V. (1982) Determination of the magnetospheric current system parameters and development of experimental geomagnetic field models based on data from *IMP* and *HEOS* satellites. *Planet. Space Sci.* **30**, 985.

Usmanov, A. V. (1984) Quantitative modeling of the magnetospheric magnetic field based on satellite data. Candidate Thesis, Leningrad University.